Published by IOP Publishing for Sissa Medialab

Received: *December 11, 2024*
Revised: *March 12, 2025*
Accepted: *April 22, 2025*
Published: *May 30, 2025*

TECHNICAL REPORT

RF design of a 1.3 GHz 3-cell superconducting cavity for high-current beam acceleration

Xuan Huang[a,b] **Xiaowei Wu**[c,*] **Jinfang Chen**[d,e,*] **Dong Wang**[d,e] **and Haixiao Deng**[d]

[a] *Shanghai Institute of Applied Physics, Chinese Academy of Sciences, Shanghai 201800, China*
[b] *University of Chinese Academy of Sciences, Beijing 100049, China*
[c] *Zhangjiang Laboratory, Shanghai 201210, China*
[d] *Shanghai Advanced Research Institute, Chinese Academy of Sciences, Shanghai 201210, China*
[e] *ShanghaiTech University, Shanghai 201210, China*

E-mail: wuxw@zjlab.ac.cn, chenjinfang@sari.ac.cn

Abstract: Superconducting radio-frequency (SRF) cavities are widely used in particle accelerator facilities. The SRF-based energy recovery linac (ERL) equipped with special SRF cavities offers feasibility for application in high-power free electron lasers (FELs). This study aims to design and optimize a 3-cell cavity that serves as the accelerating structure for a 10 mA class injector of high-brightness ERL-FEL. We apply the middle-cell shape of the mature TESLA cavity, and the end-groups are optimized for high-current beam operation. The cavity is designed with two fundamental power coupler (FPC) ports, which enable high-power input by two FPCs. In addition, the beam pipe is enlarged to damp potentially strong higher-order modes (HOMs) induced by the high current beams. A multi-objective genetic algorithm is utilized to optimize the cavity geometry. The damping of HOMs, multipacting, and mechanical issues are also investigated to verify the rationality of the cavity design.

Keywords: Acceleration cavities and superconducting magnets (high-temperature superconductor, radiation hardened magnets, normal-conducting, permanent magnet devices, wigglers and undulators); Instrumentation for particle accelerators and storage rings - low energy (linear accelerators, cyclotrons, electrostatic accelerators)

*Corresponding author.

https://doi.org/10.1088/1748-0221/20/05/T05011

Contents

1 Introduction **1**

2 RF cavity design **3**
- 2.1 Optimization algorithm 3
- 2.2 Interesting quantities 4
- 2.3 Optimization results 5

3 Further optimization **7**
- 3.1 FPC port design 7
- 3.2 HOM analysis 9
- 3.3 Multipacting investigation 13
- 3.4 Mechanical design 14

4 Conclusion **15**

1 Introduction

Superconducting radio-frequency (SRF) cavities enable high unloaded quality factor (Q_0) and high gradient field (E_{acc}). They play a key role in particle accelerators, such as light sources for biological and material science, and linear colliders for nuclear and particle physics [1]. Free electron laser (FEL) facilities can generate lasers with high brightness, short wavelengths, and strong coherence, which are a significant advance in accelerator-based light sources. Among them, FEL facilities based on SRF linac are increasingly favored due to the capability of producing high repetition-rate FEL and the gradual maturation of the technology in the last two decades. Examples include the constructed FLASH [2], E-XFEL [3], and LCLS-II [4], as well as the under-construction LCLS-II HE [5], SHINE [6], and S^{3}FEL [7]. For high-current applications, the superconducting continuous wave-based energy recovery linac (ERL) has been proposed due to its economic efficiency [8], This technology has significant potential as a next-generation high-power light source.

Recently, several ERLs based on SRF technology have been developed, such as cERL [9], EUV-FEL [10], CBETA [11], and bERLinpro [12]. Various superconducting cavities have been designed for such devices in the injector to address the issues caused by the high-current beam. The main design parameters for ERL injector cavities in the world are listed in table 1. Among them, the cERL injector cryomodule is required to accelerate the electron beam to 5 MeV, and it consists of three 1.3 GHz 2-cell superconducting cavities. The accelerating gradient of these 2-cell cavities ranges from 7.5 MV/m to 12.5 MV/m. Each cavity is equipped with two symmetrical fundamental power couplers (FPCs), which deliver up to 30 kW of power for a 10 mA beam [13]. The EUV injector comprises two cryomodules utilized in the cERL, and it is required to accelerate the electron beam to 10 MeV [10]. The Cornell ERL injector cryomodule developed for CBETA consists of five 1.3 GHz 2-cell superconducting cavities, and it is required to accelerate the electron beam to 5–6 MeV. Each cavity is equipped with two symmetrical FPCs tested up to 60 kW, and the average current has been operated at up to 65 mA in the injector [14].

2025 JINST 20 T05011

Table 1. Main design parameters for ERL-injector cavities in the world [13–15]. "SBP" stands for small beam pipe. "LBP" stands for large beam pipe.

Parameter	cERL	CBETA	bERLinpro
Design current (mA)	10	40	100
Design gradient (MV/m)	7.5–12.5	4–5	9–10
Frequency (MHz)	1300	1300	1300
Cell number	2	2	2
End iris diameter (mm)	88	78	70,78
SBP diameter (mm)	88	78	88
LBP diameter (mm)	88	88	106
R/Q (Ω)	208	222	217
G (Ω)	288	261	261
E_{pk}/E_{acc}	2.25	1.94	2.0
B_{pk}/E_{acc} (mT/(MV/m))	4.22	4.28	4.3

The ERL-based next-generation high-power light source is a promising candidate for future application. For this purpose, a high-brightness ERL-FEL has been proposed in Shanghai. The beam parameters of the ERL-FEL injector are listed in table 2 [16]. High current acceleration via SRF cavities is one of the primary technological challenges in ERL machine, which is due to the high input power and the damping of higher-order modes (HOMs) induced by the high-current beam. In this study, we propose a new 1.3 GHz SRF cavity design for the ERL injector that requires a total beam energy of 10 MeV.

Table 2. Beam parameters of the ERL-FEL injector in Shanghai.

Parameter	Value
Bunch charge (pC)	100
Bunch length, rms (mm)	0.6
Beam repetition (MHz)	100
Beam current (mA)	10
Beam energy (MeV)	10

The rest of the paper is organized as follows. In section 2, we first describe the overall consideration of the cavity design. Then, a method to optimize the cell shape based on a multi-objective genetic algorithm (MOGA) is presented, in which the main parameters are introduced as optimization objectives. In section 3, the FPC antenna is designed for high-power input to the cavity, and the diameter of the beam pipe is optimized for the damping of HOMs, in which a "U" transition connecting end-cell and the beam pipe is designed to reject the fundamental mode while allowing HOMs to pass through. Multipacting study is conducted, and mechanical design is discussed. Section 4 provides the conclusions.

2025 JINST 20 T05011

2 RF cavity design

Based on experiences in existing ERL machines [13–15], an accelerating gradient at around 10 MV/m should be a good balance for guaranteeing acceleration efficiency and addressing field emission issues.

When determining the number of cells in a cavity, the acceleration efficiency, input power limits, and the risk of HOM trapping need to be considered. A large number of cavity cells increases the compactness of an accelerator, which results in higher acceleration efficiency in energy gain at a certain length. However, this condition may introduce difficulties in FPCs and the damping of HOMs. With two symmetrical FPCs providing up to 30 kW input power, 3-cell cavities operating at 10 MV/m for 10 mA beam acceleration strike a good balance. Thus, a cryomodule with three 3-cell cavities is sufficient to provide 10 MeV acceleration in the injector section.

2.1 Optimization algorithm

Traditionally, parameter sweeping is utilized for the optimization of cavity shape. As the number of independent variables increases, the number of scans grows significantly, which complicates the classification and summarization of the optimization results. When conflict in criteria arises, multi-objective optimization methods are suited to provide a set of optimal solutions, which is called the Pareto front. Two of the most common methods for estimating the Pareto front are single-objective optimization, which combines individual objectives, and multi-objective genetic algorithms (MOGAs). The main disadvantage of the single-objective method is that it requires extensive computations to approximate the Pareto front by varying weightings. Determining the appropriate weightings may not be straightforward and can require additional time, which further complicates the optimization process. Therefore, this study employs MOGA to obtain a set of Pareto fronts. The nondominated sorting genetic algorithm (NSGA-II) [17] has been proposed to solve complex and real-world problems involving two or three objectives through elitist strategies. Based on the NSGA-II framework, the proposed NSGA-III [18, 19] is applied to optimization problems that involve four or more objectives.

The aforementioned optimization methods have been used in accelerator fields, such as photoelectron guns [20, 21], beam dynamics [22], and RF cavity design [23–26]. The input parameters, objectives, and constraints need to be iteratively verified to achieve optimal outcomes. Initially, the cavity dimensions are parameterized as the independent variable space of the algorithm, which must be defined within a suitable range to ensure computational flexibility. The electromagnetic software calculates the RF parameters of the cavity, which are subsequently used as the objective space for the algorithm. Each objective can be set for maximization or minimization based on specific requirements. Then, certain input geometric parameters or objectives must be constrained within a defined range. In this study, 2D software SUPERFISH [27] is used to calculate electromagnetic in the cavities due to its lightweight design and efficient performance. The NSGA-III serves as the main program, which provides SUPERFISH with the geometrical parameters of the cavity. After the calculation, the RF parameter results are returned to the algorithm, which are then iteratively processed.

The algorithm follows a cyclic process consisting of the following steps. First, a predefined number of populations is established. In each generation, the results are evaluated to select the nondominated solutions. Subsequently, the populations corresponding to these solutions undergo mutation and crossover to produce a new generation of populations. This process is repeated until the predefined number of generations is reached.

2025 JINST 20 T05011

2.2 Interesting quantities

The TESLA-type cavity [28] is a well-established component utilized in various large-scale superconducting accelerators. The machining and surface treatment processes of this cavity have been extensively studied, and the performances are consistently excellent. Therefore, the 3-cell cavity designed for high-current operation is based on the TESLA middle cell, with an enlarged beam pipe implemented to damp HOMs. Figure 1 shows the schematic of the cavity end-group. The geometry can be described by 11 variables: A, B, a, b, R_i, R_{eq}, L, a_U, A_U, L_U, and R_{bp}. In the optimization, R_{eq} is the same as that of the middle cell.

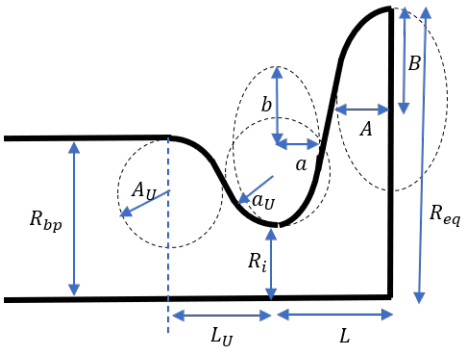

Figure 1. Schematic of an end group.

High efficiency is essential to maximize acceleration voltage while minimizing RF power losses in the cavity wall. The dynamic power loss of the fundamental mode is given by

$$P = \frac{(E_{\mathrm{acc}} \cdot L_{\mathrm{eff}})^2}{G \cdot R/Q} \cdot R_s, \tag{2.1}$$

where L_{eff} is the active length of the cavity, R_s is the surface resistance, G is the geometry factor, and R/Q is the specific shunt impedance. The accelerator definition of the R/Q is given by [29]

$$R/Q = \frac{\left|\int_{-\infty}^{\infty} E_z(\rho = 0) e^{ik_n z}\, dz\right|^2}{\omega_n U}, \tag{2.2}$$

where E_z is the longitudinal electric field at a distance of $\rho = 0$ from the beam axis, ω_n is the resonant angular frequency, k_n is the wave number, U is the stored energy, and n is the mode number. G and R/Q are independent of the cavity losses and depend only on the cavity geometry. $G \cdot R/Q$ should be maximized to minimize power losses. In addition, minimizing the peak electric field is necessary to prevent field emission. RF heating caused by the magnetic field in the cavity equator region may limit the accelerating gradient. Therefore, the ratio of the peak electric and magnetic field to the accelerating field ($E_{\mathrm{pk}}/E_{\mathrm{acc}}$ and $B_{\mathrm{pk}}/E_{\mathrm{acc}}$) needs to be minimized. Currently, three objectives related to the performance of the fundamental mode are considered. In addition, a related objective needs to be added to the damping of the HOMs, which is crucial for ensuring beam stability during high-current operation. A small end-group iris radius R_i rejects the leakage of fundamental mode but may limit the damping of HOMs. Therefore, a proper R_i is required.

Constraints are necessary in the optimization process. First, the fundamental mode of the cavity should have a fixed frequency. The frequency also needs to be controlled within a certain range

2025 JINST 20 T05011

because of the difficulty in maintaining a constant frequency. Second, $L > a + A$ must be required to avoid a reentrant shape, which complicates the chemical treatment of the cavity. The objectives and constraints in the optimization process are listed in table 3.

Table 3. Objectives and constraints in the optimization process.

Objective	Constraint
Maximize $G \cdot R/Q$	$f = 1300 \pm 1$ MHz
Minimize $E_{\mathrm{pk}}/E_{\mathrm{acc}}$	$L > a + A$
Minimize $B_{\mathrm{pk}}/E_{\mathrm{acc}}$	
Maximize R_i	

2.3 Optimization results

Reference points are required to be predefined in the NSGA-III. Many studies have used Das and Dennis' structured approach [30] to generate well-spaced reference points. The parameter p determines the number of points in the unit simplex, which indicates the number of gaps between two consecutive points along an objective axis. The total number of reference points in an M-objective problem is C^{M-1}_{M+p-1}. In this paper, $p = 12$ is used for a four-objective problem, which results in 455 reference points. The population size is chosen to be 456, which is larger than the number of reference points, to ensure accuracy.

In figure 2, the blue points present the final generation results of the four-objective optimization. R_i ranges from 35 mm to 42 mm given that the radius of the middle cell is 35 mm. A trade-off between R_i and the three other objectives is clearly observed in figure 2. A significant negative correlation exists between R_i and $G \cdot R/Q$. Conversely, a positive correlation exists between R_i and $E_{\mathrm{pk}}/E_{\mathrm{acc}}$ and $B_{\mathrm{pk}}/E_{\mathrm{acc}}$. This change may not be noticeable because the middle cell has a dominant influence. Figure 2 shows that the data points are relatively sparse because of the narrow frequency range in the constraints. As a result, some results are rounded off.

Selecting an integer value for the radius of the end-cell iris is difficult. Therefore, we fix the value of R_i to reduce the number of objectives from four to three and decrease the number of independent variables. According to the literature [25], B has a relatively small effect on RF results, and the circular structure helps mitigate multipacting, which leads to $A = B$. Thus, the total number of variables is decreased to seven. In this case, $p = 12$ is selected, which results in 91 reference points. The population size is chosen to be 92. The orange points in figure 2 show the results of the three-objective problem. Five sets of optimization results represent the last generation, with R_i ranging from 35 mm to 40 mm. The RF parameters have a similar overall trend with R_i for the three- and four-objective optimization results. The radius R_i of 39 mm has a negligible impact on the RF performance of the fundamental mode, which leads to a reduction of less than 2% compared with the R_i of 36 mm. The optimized results are $E_{\mathrm{pk}}/E_{\mathrm{acc}}$ of approximately 2 and $B_{\mathrm{pk}}/E_{\mathrm{acc}}$ of around 4.25. The requirement for minimizing the peak electromagnetic field is satisfied. The selected optimization results for the 1.3 GHz 3-cell cavity are listed in table 4. The field distribution of the fundamental mode is shown in figure 3(a) and (b). The field flatness of the cavity is shown in figure 3(c), and the accelerating gradient is normalized to 1 MV/m.

2025 JINST 20 T05011

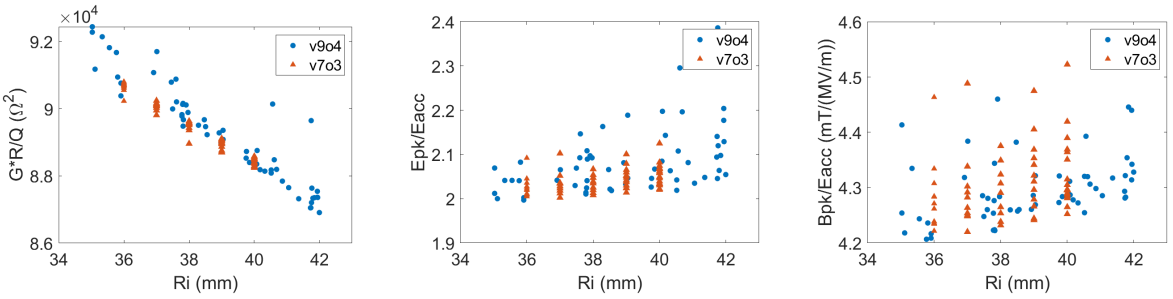

(a) (b) (c)

Figure 2. $G \cdot R/Q$ (a), $E_{\mathrm{pk}}/E_{\mathrm{acc}}$ (b), and $B_{\mathrm{pk}}/E_{\mathrm{acc}}$ (c) versus different radii of the end-cell iris. The blue points represent the final generation results of the four-objective optimization. The orange points represent the final generation results of the three-objective optimization. "v" stands for variables. "o" stands for objectives.

Table 4. Main parameters of the designed 1.3 GHz 3-cell cavity. "SBP" stands for small beam pipe. "LBP" stands for large beam pipe.

Parameter	Value
a (mm)	9
b (mm)	13.63
A (mm)	41.8
B (mm)	41.8
L (mm)	56.18
R_{eq} (mm)	103.3
R_i (mm)	39
a_U (mm)	10
A_U (mm)	35
L_U (mm)	29.48
R_{bp} (mm)	50
SBP length (mm)	130
LBP length (mm)	140
Frequency (MHz)	1300
R/Q (Ω)	329
G (Ω)	273
$E_{\mathrm{pk}}/E_{\mathrm{acc}}$	2.0
$B_{\mathrm{pk}}/E_{\mathrm{acc}}$ (mT/(MV/m))	4.27

We conduct the sensitivity analysis for the particular variables within ±0.3 mm from the goal values to evaluate the effect of geometrical variables changes on RF parameters. Meanwhile, the other variables are fixed as designed values. Figure 4 shows the sensitivity of G, R/Q, $E_{\mathrm{pk}}/E_{\mathrm{acc}}$, and $B_{\mathrm{pk}}/E_{\mathrm{acc}}$ versus the five geometrical parameters. When the geometrical variables change by 0.3 mm, the variations in RF parameters are less than 3%. A is the relatively most sensitive variable to $B_{\mathrm{pk}}/E_{\mathrm{acc}}$. Thus, we can pay close attention to the equatorial elliptic contour during the fabrication process. The designed values of the cavity are optimal results according to figure 4.

2025 JINST 20 T05011

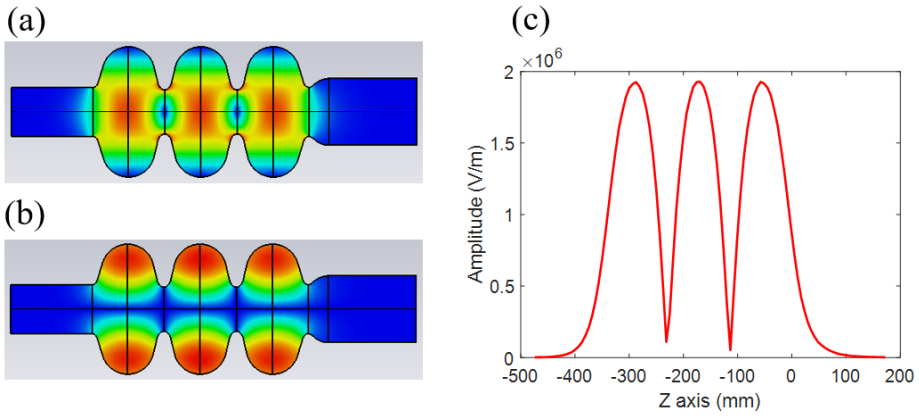

Figure 3. Electric (a) and magnetic (b) field distribution, and field flatness (c) of the fundamental mode.

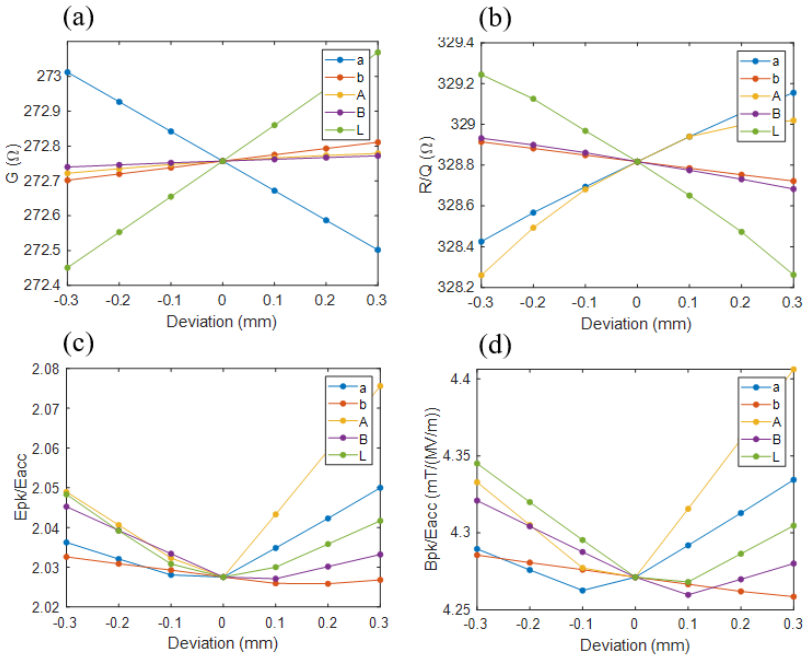

Figure 4. Sensitivity analysis for the main geometrical variables.

3 Further optimization

3.1 FPC port design

We adopt coaxial-type FPCs to input the RF power into the cavity because of their compactness and adjustability of external quality factor. A symmetric dual-feeding configuration is implemented for the cavity to minimize the RF kick effect. The external quality factor Q_e of the FPC antenna can be calculated according to the following formula:

$$Q_e = \frac{E_{\text{acc}} \cdot L_{\text{eff}}}{R/Q \cdot I}. \tag{3.1}$$

For instance, operating at 12 MV/m for a 10 mA electron beam requires an optimal $Q_e = 1.23 \times 10^6$.

2025 JINST 20 T05011

Two improvements are implemented to enhance coupling compared with the FPC used in the TESLA cavity. First, a coaxial line of 62 mm and 60 Ω is used instead of the TESLA FPC with a coaxial line of 40 mm and 70 Ω. Second, the tip of the antenna is designed in the shape of a bending disc. The shape of the antenna is shown in figure 5. Next, we optimize the elliptical dimensions of the tip. Figure 6 shows Q_e versus the tip dimension. The optimal coupling occurs when the elliptical disc is at $R_x = 23$ mm and $R_y = 18$ mm.

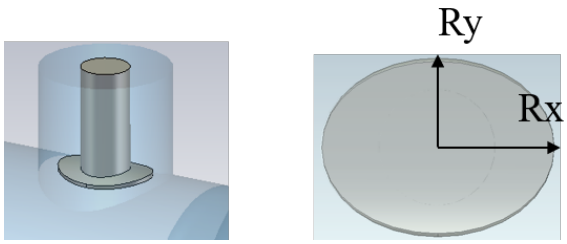

Figure 5. Shape of the antenna for the FPC.

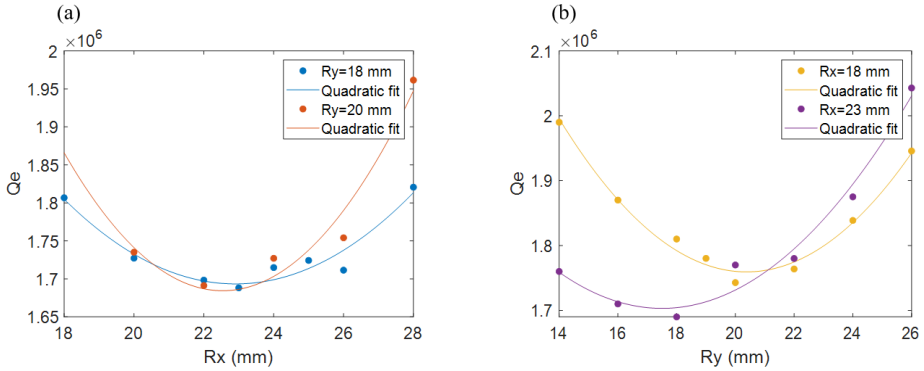

Figure 6. (a) Q_e versus the elliptical dimensions R_x. (b) Q_e versus the elliptical dimensions R_y. The solid circles indicate the simulation results. The solid lines indicate a quadratic fit.

The coupling of the antenna is also affected by the distance between the FPC port and the end-cell iris. When the FPC port is positioned farther away from the end-cell iris, the bottom of the antenna must be closer to the beam center to attain equivalent coupling effects. Consequently, minimizing the gap between the FPC port and the end-cell iris is imperative, while sufficient clearance for the placement of the reference ring needs to be guaranteed. However, this distance should not be less than 20 mm considering the fabrication difficulty.

Figure 7 shows the antenna insertion depth and $B_{\mathrm{pk}}/E_{\mathrm{acc}}$ at the antenna versus the distance, and each point satisfies the optimal coupling requirement. Figure 7(a) shows that the double-enlarged beam pipe structure necessitates a distance of less than 16 mm to avoid the antenna penetrating the interior of the beam pipe, Therefore, it does not meet the fabrication requirement. Accordingly, a structure with single-enlarged beam pipe on one side is proposed, with the radius of the beam pipe on the non-enlarged side matching that of the end-cell iris. The FPC is placed on the non-enlarged side of the beam pipe. Similarly, a scan is conducted to determine the FPC distance for the single-enlarged beam pipe structure. Figure 7(b) shows that the distance can extend up to 25 mm before the antenna tip down to the interior of the beam pipe. Thus, the single-enlarged beam pipe structure is adopted,

2025 JINST 20 T05011

and 20 mm is chosen for the distance between the FPC port and the end-cell iris. Consequently, the bottom of the antenna is positioned 6 mm away from the edge of the beam pipe in this scenario.

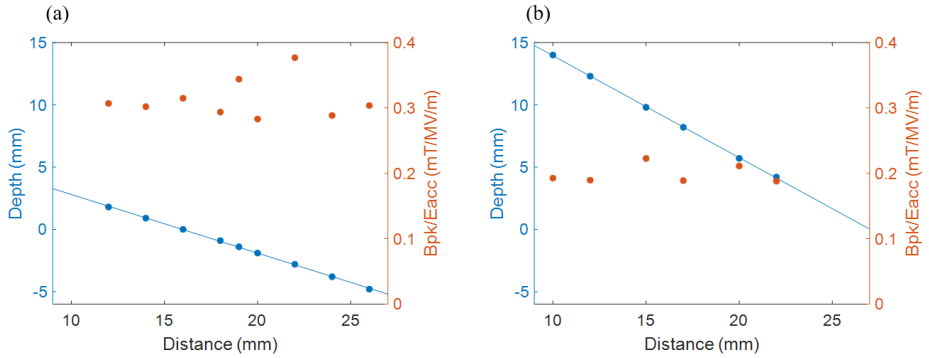

Figure 7. Antenna insertion depth (left axes) and $B_{\mathrm{pk}}/E_{\mathrm{acc}}$ (right axes) at the antenna versus different distances between the FPC port and the end-cell iris for the double-enlarged beam pipe structure (a) and the single-enlarged beam pipe structure (b). The solid lines indicate a linear fit.

3.2 HOM analysis

Wakefields can be excited by the beam passing through the cavity, which can be classified into two types: the longitudinal and transverse ones. The longitudinal wakefields may increase the energy spread of the bunch and lead to power loss in the cavity wall. The transverse wakefields degrades the emittance of the bunch, and may potentially result in beam break up (BBU) in severe cases. These effects are more severe for high-current operation, in which the damping of HOMs becomes significantly important. Considering the multi-bunch cavity interaction, resonant HOMs may occur when the HOM frequencies are harmonics of the bunch frequency. The maximum power loss in a general case of HOM excitation can be expressed by [31]

$$\langle P \rangle_{\mathrm{max}} = \frac{R/Q\omega_n q_0^2}{4t_b}\left(\frac{e^{\alpha}+1}{e^{\alpha}-1}\right), \tag{3.2}$$

where q_0 is the bunch charge, t_b is the bunch spacing, $\alpha = t_b/\tau$, and $\tau = 2Q_e/\omega_n$ is the HOM decay time. If $t_b < \tau$, then equation (3.2) leads to a resonant HOM excitation. The power in the worst-case scenario can be simplified to $I^2 \cdot R/Q \cdot Q_e$, where I is the average beam current, which is 10 mA for this facility. If $t_b > \tau$, then a non-resonant single-bunch excitation occurs. In this case, equation (3.2) can be reduced to $k_{\parallel} q_0 I$, where $k_{\parallel}$ is the loss factor. Next, we use the worst-case power to obtain the longitudinal threshold impedance $Q_e \times R/Q$ [32]. Assuming approximately 100 W of absorption can be fulfilled, the product $Q_e \times R/Q$ of monopole HOMs would be less than $1 \times 10^6\ \Omega$.

The damping of dipole modes is related to the BBU threshold current. Given that the injector section is not located inside the recirculation loop, no multi-turn BBU effect is exerted in these injector cavities. Therefore, the single-pass threshold current can be estimated using the following equation [33]:

$$I_{\mathrm{th}} = \frac{\pi^3 V_{\mathrm{beam}}}{2R_{\perp}/Q \cdot Q_e \cdot L_{\mathrm{eff}}} F(x), \tag{3.3}$$

where V_{beam} is the exit beam energy as delivered from the cavities, $F(x)$ is a correction factor for acceleration from an initial momentum to a final momentum, and $R_{\perp}/Q$ is the specific transverse

2025 JINST 20 T05011

shunt impedance [29]:

$$R_\perp/Q = \frac{\left|\int_{-\infty}^{\infty} E_z(\rho = r)e^{ik_n z}\, dz\right|^2}{r^2\omega_n U} \cdot \frac{1}{k_n}, \tag{3.4}$$

where E_z is the longitudinal electric field at a distance of $\rho = r$ from the beam axis. $R_\perp/Q$ is calculated at the offset of 1 mm, with the unit of Ω/cm. $F(x)$ can be expressed as

$$F(x) = \frac{(x-1)^3}{6x\left[(x-1)^2/2 + x - 1 - x\ln(x)\right]}, \tag{3.5}$$

where x is the ratio of a final momentum to an initial momentum. In this case, the exit energy of the VHF gun is around 720 keV, and the same energy gain of 3.3 MeV is assumed for each cavity in the injector. Subsequently, the lowest transverse threshold impedance $Q_e \times R_\perp/Q$ can be calculated as 9.5×10^7 Ω/cm.

In this study, CST [34] lossy eigenmode solver is used to calculate the shunt impedance and external quality factor Q_e of HOMs. We use two different methods to conduct the simulation. First, open boundary conditions are applied to beam pipes and FPC ports as a start point. Second, beam pipes and FPC ports are terminated with HOM absorbers and waveguide ports, respectively. The designed length of the absorber ceramic is 50 mm, with a thickness of 10 mm. The real part permittivity of 50 and the loss tangent of 0.1 are used for the HOM absorber material, which can be achieved for common AlN or SiC materials. Figure 8 shows the cavity and boundary conditions utilized in the lossy eigenmode solver.

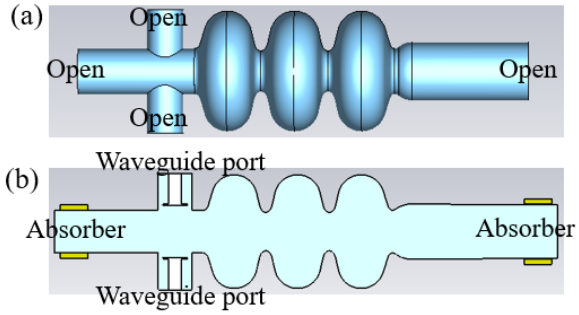

Figure 8. Cavity model with open boundary (a) and HOM absorbers (b) for the simulation of HOMs.

First, we conduct shunt impedance simulations using the boundary conditions in figure 8(a) as a start point. As shown in figure 9, a comparison of the shunt impedance of HOMs is conducted for the R_i values of 36 and 39 mm. The highest $Q_e \cdot R/Q$ of the monopole TM011 mode for the R_i values of 36 and 39 mm are 7.1×10^4 Ω at 2454 MHz and 5.2×10^4 Ω at 2444 MHz, respectively. The cutoff frequency of TM01 is 2086 MHz corresponding to a beam pipe diameter of 110 mm. HOMs near the cutoff frequency require particular attention. Selecting an R_i value of 39 mm is advisable to obtain a lower shunt impedance of TM011 mode. Notably, the longitudinal shunt impedance of all modes is below the longitudinal threshold impedance of 1×10^6 Ω. The highest $Q_e \cdot R_\perp/Q$ of the dipole TM110 mode for the R_i values of 36 and 39 mm are 2.1×10^4 Ω/cm at 1887 MHz and 1.3×10^4 Ω/cm at 1886 MHz, respectively. The cutoff frequency of TE11 is 1597 MHz corresponding to a beam pipe diameter of 110 mm. Similarly, selecting an R_i value of 39 mm is suggested to obtain

2025 JINST 20 T05011

a lower shunt impedance of TM110 mode. The transverse shunt impedance for all dipole modes is significantly below the transverse threshold impedance of 9.5×10^7 Ω/cm.

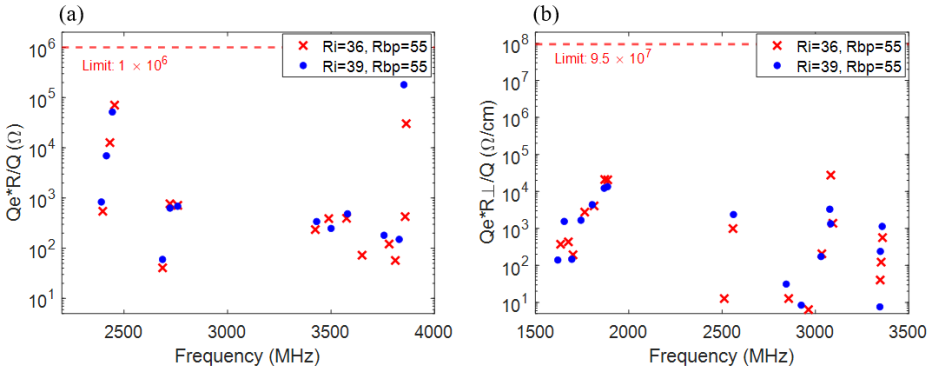

Figure 9. Comparison of the impedance spectrum of HOMs for the R_i values of 36 and 39 mm with a beam pipe diameter of 110 mm. (a) Shunt impedance of monopole HOMs. (b) Shunt impedance of dipole HOMs.

The RF loss of the fundamental mode at the absorber region should be well controlled through selecting a proper end-group iris. A large end-group iris and beam pipe diameter will lead to a long beam pipe to attenuate the RF power. The shunt impedance of HOMs exhibits a margin that allows for a reduction in beam pipe diameter. Figure 10 shows the shunt impedance of HOMs for beam pipe diameters of 100, 106, and 110 mm. The highest shunt impedance of the monopole TM011 mode for a beam pipe diameter of 100 mm is 8.6×10^4 Ω at 2454 MHz, which is higher than other cases but below the longitudinal threshold impedance of 1×10^6 Ω. The HOM power of the TM011 mode reaches 8.6 W if the frequency is synchronized with the beam harmonic. The highest shunt impedance of the dipole TE111 mode for a beam pipe diameter of 100 mm is 8.5×10^4 Ω/cm at 1667 MHz, This impedance is higher than other cases but smaller than the transverse threshold impedance of $9.5 \times 10^7\ \Omega/cm$. Therefore, a beam pipe diameter of 100 mm strikes a good balance.

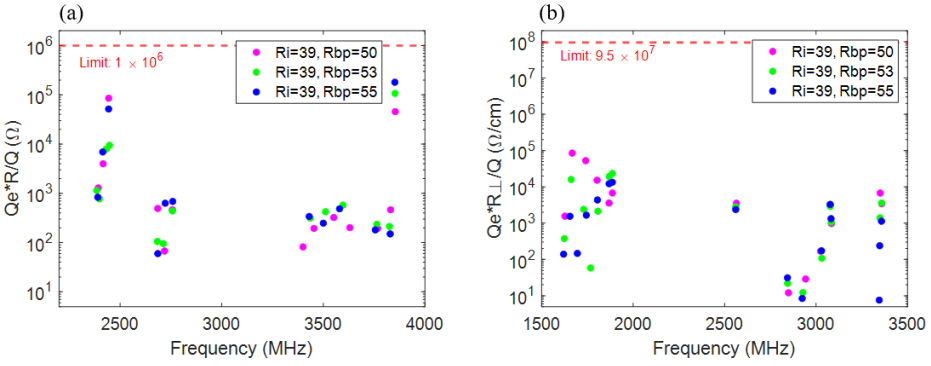

Figure 10. Comparison of the impedance spectrum of HOMs for the beam pipe diameters of 100, 106, and 110 mm. (a) Shunt impedance of monopole HOMs. (b) Shunt impedance of dipole HOMs.

After the proper R_i and beam pipe diameter of the cavity are obtained, we conduct shunt impedance simulations using the conditions in figure 8(b) to mimic the cavity in the cryomodule, where the HOMs absorbers and FPCs are equipped. During the simulation, the dielectric loss is induced by the absorbing materials. In this case, the position of HOM absorbers is optimized such that the RF loss of

2025 JINST 20 T05011

the fundamental mode is less than 1% of the cavity wall loss. Then, the shunt impedance of HOMs is simulated with absorbers, as shown in figure 11. The highest shunt impedance of the monopole TM011 mode is 2.7×10^5 Ω at 2444 MHz, which is around 3.2 times higher than that in the simulation with open boundary conditions. Notably, the second mode in the fundamental pass band is 1.2×10^5 Ω at 1294 MHz, which is relatively high but lower than the longitudinal threshold impedance of 1×10^6 Ω. The highest shunt impedance of the dipole TE111 mode is 1.9×10^5 Ω/cm at 1667 MHz, which is around 2.2 times higher than the one with open boundary conditions. The shunt impedances of dipole modes are much less than the limit of the transverse threshold impedance of 9.5×10^7 Ω/cm.

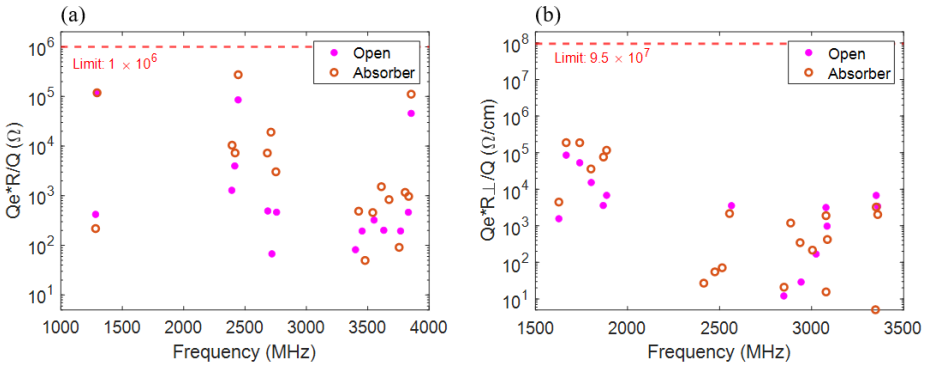

Figure 11. Comparison of the impedance spectrum of HOMs between open and absorbers conditions. (a) Shunt impedance of monopole HOMs (except accelerating mode). (b) Shunt impedance of dipole HOMs.

The power of resonant HOMs is calculated by equation (3.2), as shown in figure 12(a). The maximum resonant power is 12 W with HOM absorbers. Nevertheless, the frequencies of HOMs are far from the beam harmonics, and the damping of HOMs is sufficiently satisfied. In addition, the non-resonant losses are related to the longitudinal wakefield by a single bunch. Figure 12(b) shows the longitudinal short-range wakefield calculated by ECHO [35] for a bunch length of 0.6 mm. The bunch enters through the large beam pipe during the simulation. The loss factor is 4.5 V/pC, and the non-resonant power loss is 4.5 W using the bunch parameters listed in table 2, which is lower than the resonant case.

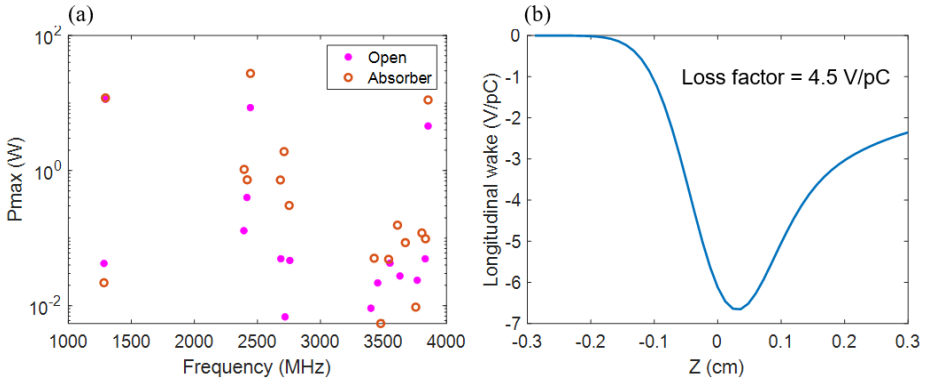

Figure 12. (a) Power of resonant HOMs (except accelerating mode). (b) Longitudinal short-range wakefield corresponding to non-resonant losses.

3.3 Multipacting investigation

The impact of multipacting on the performance of superconducting cavities has been extensively investigated in the TESLA-shaped superconducting cavities. Secondary electrons emit when the secondary electron yield (SEY) exceeds 1, and multipacting will occur when these electrons establish a stable trajectory in a specific region. Multipacting is usually referred to a soft barrier that can be mitigated by RF processing in elliptical cavities. However, a different design may bring hard barrier that leads to cavity quench by thermal breakdown at the affected locations. Therefore, the potential risk of multipacting associated with cavity geometry should be investigated to check the rationality of the cavity design. SEY also depends on material surface conditions. In this study, the simulations are based on cryogenic SEY data of a niobium sample from the literature [36]. The niobium sample was treated by buffered chemical polishing and annealing at 900°C under vacuum (10^{-4} Pa). Figure 13 shows the SEY curve of the niobium sample.

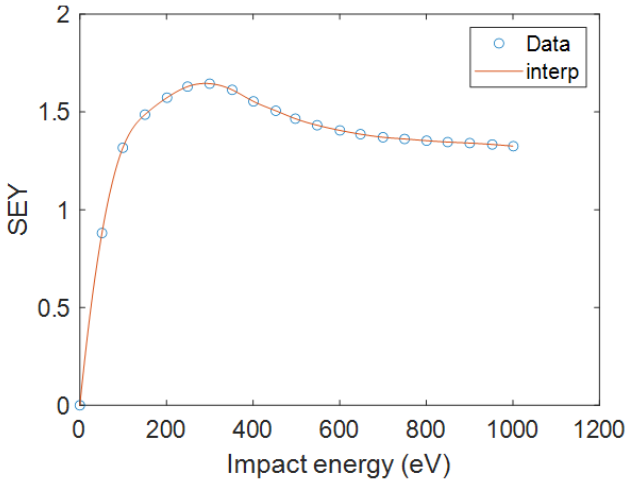

Figure 13. SEY versus impact energy. The open circles indicate the measured results. The solid line indicates interpolation. Reprinted from [36], Copyright (2022), with permission from Elsevier.

The region where multipacting occurs in the TESLA-shaped cavity is usually at the equator. Simulations and experiments demonstrate that multipacting in the TESLA cavity primarily occurs from 16 MV/m to 24 MV/m [37]. The vertical test of the Cornell ERL 2-cell cavity indicates the occurrence of multipacting, with simulations demonstrating that the presence of electric field troughs in the transition segments is responsible for this phenomenon [38, 39]. Consequently, the structure of transition segments requires further optimization to mitigate multipacting. In the initial phase of the optimization process, a transition consisting of two circular arcs connected by a straight segment is utilized, which is similar to a cell profile. The optimization process results in a narrow arc for the section connecting to the beam pipe. Subsequently, we adopt a new profile in which two circular arcs are connected without a straight segment. Therefore, the transition can be described by four parameters: a_U, A_U, R_i, and R_{bp}. Then, L_U can be calculated by

$$L_U = \sqrt{(a_U + A_U)^2 - \left(R_i + a_U + A_U - R_{\mathrm{bp}}\right)^2}. \tag{3.6}$$

2025 JINST 20 T05011

The point of tangency between two circles can be expressed as

$$x_p = L_U \cdot \frac{a_U}{a_U + A_U},$$
$$y_p = R_i - a_U \cdot \frac{R_i - R_{\text{bp}}}{a_U + A_U}. \tag{3.7}$$

Therefore, we have two independent parameters (a_U and A_U) for optimization with $R_i = 39\,\text{mm}$ and $R_{\text{bp}} = 100\,\text{mm}$.

A model consisting of an end-half cell and the transition is utilized to investigate the impact of the transition on multipacting. CST [34] Particle-In-cell (PIC) and eigenmode solvers are used for multipacting simulation. A quarter model is implemented to keep computational resources feasible. The electromagnetic fields of the cavity are first calculated using the eigenmode solver and then imported into the PIC solver. Figure 14 shows the electron emission source utilized in the simulation. The initial electron energy range is set between 1.5 and 4.5 eV, with an electron emission angle of 45°. The calculation takes approximately 40 RF cycles. The number of particles over time can be expressed as $N = N_0 e^{\alpha t}$, where t is the RF time, N_0 is the initial electron, and N is the total electron. The growth rate α is calculated by fitting the data. A value of α greater than zero indicates that multipacting is likely to occur.

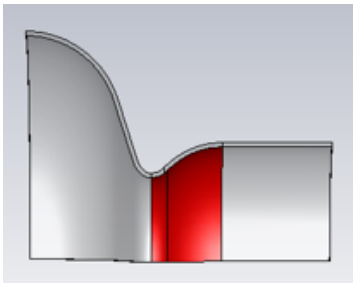

Figure 14. Model was utilized for multipacting simulation. The red region presents an electron emission source.

In the simulation, a_U is maintained at a constant value of 10 mm, while A_U is increased from 5 mm to 35 mm. The growth rate is calculated under different accelerating gradients, as shown in figure 15. The growth rate is below zero at the desired gradient of 12 MV/m when A_U exceeds 10 mm. A_U is set to 35 mm to facilitate a smoother transition. Consequently, the potential risk of multipacting associated with the cavity structure is effectively eliminated.

3.4 Mechanical design

Figure 16 shows the mechanical model of the bare 1.3 GHz 3-cell cavity based on the abovementioned RF design. The wall thickness of the cavity is 2.8 mm, and the thickness of the stiffening ring is 3 mm. The mechanical structure of the cavity is optimized to reduce helium pressure sensitivity (df/dp) [40], which is regarded as the main contributor to the microphone effect. The primary method is to add stiffening rings between adjacent cells, as well as end discs. The radius of the stiffening ring is selected as 70 mm for relatively low df/dp, while a reasonable hardness is ensured such that the cavity remains tunable. The simulated df/dp is 33.5 Hz/mbar with the tuner stiffness of 40 kN/mm. The simulated tuning sensitivity is 0.9 MHz/mm, and the stiffness of the cavity with helium vessel is 46 kN/mm. After optimization, the mechanical performance of the cavity meets the requirement.

2025 JINST 20 T05011

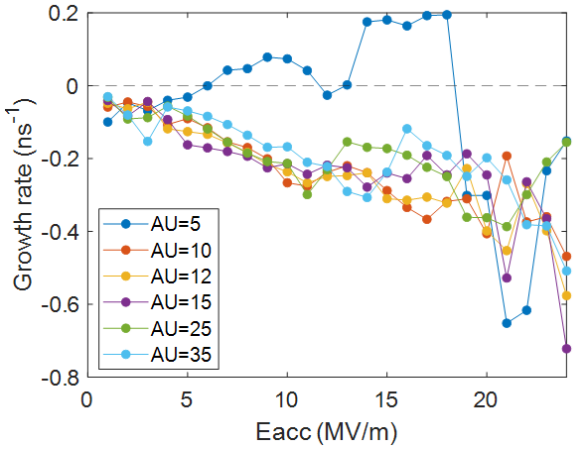

Figure 15. Growth rate versus E_{acc} at different A_U.

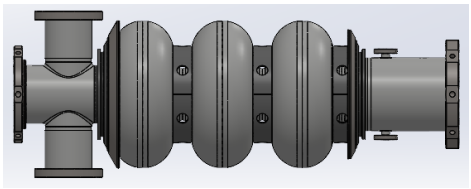

Figure 16. Mechanical model of the 1.3 GHz 3-cell cavity.

4 Conclusion

We propose a new design of a 3-cell SRF cavity dedicated for 10 mA class high-current beam acceleration in an ERL injector by using a MOGA. The cavity is designed with similar peak electric and magnetic field to the TESLA cavity, which has been proven successful by thousands of cavities in the world. This technology has now matured to achieve high gradient and free field emission for FEL applications. The beam pipes and coupler ports are designed to provide sufficient external quality factor for power input and HOM damping. Multipacting simulations and mechanical design are conducted to verify the feasibility of the cavity design. In the future, prototypes will be fabricated based on this design.

Acknowledgments

This work was supported by the National Key Research and Development Program of China (2024YFA1612101), National Natural Science Foundation of China (12125508), and Shanghai Pilot Program for Basic Research – Chinese Academy of Sciences, Shanghai Branch (JCYJ-SHFY-2021-010).

References

[1] H. Padamsee, *50 years of success for SRF accelerators—a review*, *Supercond. Sci. Technol.* **30** (2017) 053003.

[2] W. Ackermann et al., *Operation of a free-electron laser from the extreme ultraviolet to the water window*, *Nature Photon.* **1** (2007) 336.

2025 JINST 20 T05011

[3] W. Decking et al., *A MHz-repetition-rate hard X-ray free-electron laser driven by a superconducting linear accelerator*, *Nature Photon.* **14** (2020) 391.

[4] LCLS-II collaboration, *The Linac Coherent Light Source-II Project*, in the proceedings of the *5th International Particle Accelerator Conference*, Dresden, Germany, June 16–20 (2014) [DOI:10.18429/JACoW-IPAC2014-TUOCA01].

[5] T. Raubenheimer, *The LCLS-II-HE, A High Energy Upgrade of the LCLS-II*, in the proceedings of the *60th ICFA Advanced Beam Dynamics Workshop on Future Light Sources*, Shanghai, China, March 5–9 (2018) [DOI:10.18429/JACoW-FLS2018-MOP1WA02].

[6] Z. Zhao, D. Wang, Z.-H. Yang and L. Yin, *SCLF: An 8-GeV CW SCRF Linac-Based X-Ray FEL Facility in Shanghai*, in the proceedings of the *38th International Free-Electron Laser Conference*, Santa Fe, U.S.A., August 20–25 (2017) [DOI:10.18429/JACoW-FEL2017-MOP055].

[7] W.Q. Zhang, *Shenzhen Superconducting Soft X-ray Free Electron Laser (S3FEL)*, presented at the *21st International Conference on RF Superconductivity*, Grand Rapids, MI, U.S.A., June 25–30 (2023).

[8] I. Ben-Zvi, *Superconducting energy recovery linacs*, *Superconductor Science and Technology* **29** (2016) 103002.

[9] M. Akemoto et al., *Construction and commissioning of the compact energy-recovery linac at KEK*, *Nucl. Instrum. Meth. A* **877** (2018) 197.

[10] H. Kawata et al., *High power light source for future extreme ultraviolet lithography based on energy-recovery linac free-electron laser*, *J. Micro/Nanopattern. Mater. Metrol.* **21** (2022) 021210.

[11] A. Bartnik et al., *CBETA: First Multipass Superconducting Linear Accelerator with Energy Recovery*, *Phys. Rev. Lett.* **125** (2020) 044803.

[12] A. Neumann et al., *bERLinPro Becomes SEALab: Status and Perspective of the Energy Recovery Linac at HZB*, in the proceedings of the *13th International Particle Accelerator Conference*, Bangkok, Thailand, June 17–20 (2022), pp. 1110–1113 [DOI:10.18429/JACoW-IPAC2022-TUPOPT048].

[13] K. Watanabe et al., *Development of the superconducting rf 2-cell cavity for cERL injector at KEK*, *Nucl. Instrum. Meth. A* **714** (2013) 67.

[14] B. Dunham et al., *Record high-average current from a high-brightness photoinjector*, *Appl. Phys. Lett.* **102** (2013) 034105.

[15] A. Burrill et al., *First Test Results of the BERLinPro 2-cell Booster Cavities*, in the proceedings of the *6th International Particle Accelerator Conference*, Richmond, U.S.A., May 3–8 (2015) [DOI:10.18429/JACoW-IPAC2015-WEPMA010].

[16] X. Chen et al., *The design of high-brightness ERL-FEL injector based on VHF electron gun*, *Nucl. Instrum. Meth. A* **1070** (2025) 170058 [arXiv:2410.17660].

[17] K. Deb, A. Pratap, S. Agarwal and T. Meyarivan, *A fast and elitist multiobjective genetic algorithm: NSGA-II*, *IEEE Trans. Evol. Comput.* **6** (2002) 182.

[18] K. Deb and H. Jain, *An Evolutionary Many-Objective Optimization Algorithm Using Reference-Point-Based Nondominated Sorting Approach, Part I: Solving Problems With Box Constraints*, *IEEE Trans. Evol. Comput.* **18** (2014) 577.

[19] H. Jain and K. Deb, *An Evolutionary Many-Objective Optimization Algorithm Using Reference-Point Based Nondominated Sorting Approach, Part II: Handling Constraints and Extending to an Adaptive Approach*, *IEEE Trans. Evol. Comput.* **18** (2014) 602.

[20] I.V. Bazarov and C.K. Sinclair, *Multivariate optimization of a high brightness dc gun photoinjector*, *Phys. Rev. ST Accel. Beams* **8** (2005) 034202.

2025 JINST 20 T05011

[21] T. Luo et al., *RF design of APEX2 two-cell continuous-wave normal conducting photoelectron gun cavity based on multi-objective genetic algorithm*, *Nucl. Instrum. Meth. A* **940** (2019) 12 [arXiv:1905.10619].

[22] J. Yan and H. Deng, *Generation of large-bandwidth x-ray free electron laser with Evolutionary Many-Objective Optimization Algorithm*, *Phys. Rev. Accel. Beams* **22** (2019) 020703 [arXiv:1806.04993].

[23] Z. Tang, Y. Pei and J. Pang, *Optimal design of a standing-wave accelerating tube with a high shunt impedance based on a genetic algorithm*, *Nucl. Instrum. Meth. A* **790** (2015) 19.

[24] M. Kranjcevic et al., *Multi-objective shape optimization of radio frequency cavities using an evolutionary algorithm*, *Nucl. Instrum. Meth. A* **920** (2019) 106 [arXiv:1810.02990].

[25] M. Kranjčević et al., *Constrained multiobjective shape optimization of superconducting rf cavities considering robustness against geometric perturbations*, *Phys. Rev. Accel. Beams* **22** (2019) 122001 [arXiv:1905.13693].

[26] S. Smith et al., *Multiobjective optimization and Pareto front visualization techniques applied to normal conducting rf accelerating structures*, *Phys. Rev. Accel. Beams* **25** (2022) 062002.

[27] K. Halbach and R.F. Holsinger, *Superfish -A computer program for evaluation of RF cavities with cylindrical symmetry*, *Part. Accel.* **7** (1976) 213.

[28] B. Aune et al., *The superconducting TESLA cavities*, *Phys. Rev. ST Accel. Beams* **3** (2000) 092001 [physics/0003011].

[29] H. Padamsee, J. Knobloch and T. Hays, *RF Superconductivity for Accelerators*, Wiley Series in Beam Physics and Accelerator Technology, Wiley-VCH, Weinheim (1998).

[30] I. Das and J.E. Dennis, *Normal-Boundary Intersection: A New Method for Generating the Pareto Surface in Nonlinear Multicriteria Optimization Problems*, *SIAM J. Optim.* **8** (1998) 631.

[31] A. Lunin et al., *Resonant excitation of high order modes in the 3.9 GHz cavity of the Linac Coherent Light Source*, *Phys. Rev. Accel. Beams* **21** (2018) 022001.

[32] M. Liepe, *Conceptual Layout of the Cavity String of the Cornell ERL Main Linac Cryomodule*, in the proceedings of the *11th Workshop on RF Superconductivity*, Lübeck/Travemünde, Germany, September 8–10 (2003), pp. 115–119.

[33] T.P. Wangler, *RF Linear Accelerators*, Wiley (2008) [DOI:10.1002/9783527623426].

[34] *CST Studio Suite*, https://www.3ds.com/products/simulia/cst-studio-suite.

[35] I. Zagorodnov and T. Weiland, *TE/TM field solver for particle beam simulations without numerical Cherenkov radiation*, *Phys. Rev. ST Accel. Beams* **8** (2005) 042001.

[36] J. Fang et al., *Cryogenic secondary electron yield measurements on structural materials applied in particle accelerators*, *Nucl. Instrum. Meth. A* **1027** (2022) 166292.

[37] V. Shemelin, *Multipactor in crossed rf fields on the cavity equator*, *Phys. Rev. ST Accel. Beams* **16** (2013) 012002.

[38] P. Barnes et al., *Manufacture and Performance of Superconducting RF Cavities for Cornell ERL Injector*, *Conf. Proc. C* **070625** (2007) 2340.

[39] S. Belomestnykh and V. Shemelin, *Multipacting-free transitions between cavities and beam-pipes*, *Nucl. Instrum. Meth. A* **595** (2008) 293.

[40] X. Huang et al., *1.3 GHz 3-cell superconducting cavity for high current beam acceleration*, presented at the *Workshop on Energy Recovery Linacs*, Tsukuba, Japan, September 24–27 (2024).

2025 JINST 20 T05011